

Resolving the puzzle of type IIP SN 2016X

V. P. Utrobin^{1,2*} and N. N. Chugai³

¹*NRC “Kurchatov Institute” – Institute for Theoretical and Experimental Physics, B. Cheremushkinskaya St. 25, 117218 Moscow, Russia*

²*Max-Planck-Institut für Astrophysik, Karl-Schwarzschild-Str. 1, 85748 Garching, Germany*

³*Institute of Astronomy, Russian Academy of Sciences, Pyatnitskaya St. 48, 119017 Moscow, Russia*

Accepted XXX. Received YYY; in original form ZZZ

ABSTRACT

The enigmatic type IIP SN 2016X demonstrates the unprecedented asphericity in the nebular H α line profile, the absence of nebular [O I] emission, and the unusual occultation effect due to the internal dust. The hydrodynamic modelling of the bolometric light curve and expansion velocities suggests that the event is an outcome of the massive star explosion that ejected $28 M_{\odot}$ with the kinetic energy of 1.7×10^{51} erg and $0.03 M_{\odot}$ of radioactive ^{56}Ni . We recover the bipolar distribution of ^{56}Ni from the H α profile via the simulation of the emissivity produced by non-spherical ^{56}Ni ejecta. The conspicuous effect of the dust absorption in the H α profile rules out the occultation by the dusty sphere or dusty thick disk but turns out consistent with the thin dusty disk-like structure in the plane perpendicular to the bipolar axis. We speculate that the absence of the nebular [O I] emission might originate from the significant cooling of the oxygen-rich matter mediated by CO and SiO molecules.

Key words: hydrodynamics – methods: numerical – supernovae: general – supernovae: individual: SN 2016X

1 INTRODUCTION

Type IIP supernovae (SNe IIP, “P” stands for plateau at the light curve) originate from massive stars that retain a significant fraction of the hydrogen envelope until the core collapse. A pre-SN star before the explosion has the structure of a red supergiant (RSG) (Grassberg et al. 1971; Smartt 2009) which favors the high luminosity at the plateau powered by the explosion energy. The plateau with a duration of about 100 days is followed by the radioactive tail which, in turn, is powered by ^{56}Co decay. SNe IIP show a broad range of plateau luminosities: from $\sim 2 \times 10^{41}$ erg s⁻¹ for sub-luminous SNe IIP, e.g., SN 2003Z (Utrobin et al. 2007), to $\sim 10^{43}$ erg s⁻¹ for SN 2009kf, the most energetic case among ordinary SNe IIP (Utrobin et al. 2010). SN 1987A-like supernovae related to the explosion of a blue supergiant (BSG) sometimes are classified as peculiar SNe IIP, although their broad luminosity maximum at about 90–100 days is completely powered by the radioactive decay of ^{56}Co (Woosley 1988).

According to the evolutionary models, SNe IIP originate from the progenitors in the range of $9 - M_{\text{IIP}}$ with $M_{\text{IIP}} \approx 25 M_{\odot}$ for solar metallicity and $M_{\text{IIP}} \approx 40 M_{\odot}$ for low metallicities (Heger et al. 2003). The hydrodynamic modelling of the well-observed SNe IIP recovers the ejecta masses in the range of $13.1\text{--}28.1 M_{\odot}$ for the sample of 10 SNe IIP

(Utrobin & Chugai 2017). This is in line with the ejecta mass range of $12.4\text{--}25.6 M_{\odot}$ for the sample of 9 SNe IIP, inferred by Nadyozhin (2003) using the scaling relations based on the hydrodynamic models (Litvinova & Nadezhin 1985). These “hydrodynamic” ejecta masses combined with the neutron star mass lead to the minimum progenitor masses in the range of $14\text{--}30 M_{\odot}$ without taking into account the mass loss. A comparison of the archive photometry of SN IIP progenitors with the evolutionary RSG models indicates the lower progenitor masses of $8\text{--}18 M_{\odot}$ (Smartt 2015), that brings about yet unsettled tension between the hydrodynamic masses and the masses recovered from the archival photometry (but see e.g. Pumo et al. 2017).

There is a general consensus that the SN IIP explosion is caused by the core collapse, although the conversion of the binding energy of a newly born neutron star into the kinetic energy of the ejecta is not yet fully understood. The preferred mechanism is the neutrino-driven explosion, however the successful self-consistent model is available so far only for low energy ($\approx 10^{50}$ erg) events related to $\approx 10 M_{\odot}$ progenitors (Janka 2017). The general physical arguments admit that the neutrino-driven explosion is able to provide the energy of up to 2×10^{51} erg (Janka 2017). The alternative mechanism is the magneto-rotational explosion driven by either magnetic bipolar jets (LeBlanc & Wilson 1970; Wheeler et al. 2002; Bisnovatyi-Kogan et al. 2018), or by amplified toroidal field along the equatorial plane (Bisnovatyi-Kogan 1971; Bisnovatyi-Kogan et al. 2018). The

* E-mail: utrobin@itep.ru

intrinsic feature of the magneto-rotational explosion seems to be a bipolar ejecta asymmetry. Another remarkable property of the magneto-rotational mechanism is its potential to produce the high-energy events (Burrows et al. 2007) that could account for SN 2009kf with the explosion energy of 2.15×10^{52} erg (Utrobin et al. 2010).

The magneto-rotational explosion of SNe IIP thus might be indicated by the high explosion energy and the ejecta asymmetry. The explosion energy of SNe IIP along with the ejecta mass and the pre-SN radius can be recovered only via the modelling of the light curve and expansion velocities of the well-observed objects. As to the explosion asymmetry, it could be imprinted in the asphericity of the ^{56}Ni ejecta. The latter, in turn, can be revealed via the $H\alpha$ asymmetry at the nebular stage when the line emissivity closely traces the energy deposition of gamma-rays and positrons from the ^{56}Co decay (Chugai 2007).

Until recently the most conspicuous $H\alpha$ asymmetry in SNe IIP was demonstrated by SN 2004dj (Chugai et al. 2005) and was interpreted as an outcome of the bipolar ^{56}Ni ejecta. Less pronounced, yet apparent, is the asymmetry of SN 2013ej (Mauerhan et al. 2017) that shows signatures of the asymmetric high-velocity ^{56}Ni ejecta (Utrobin & Chugai 2017). The asymmetry shown by the recent type IIP SN 2016X (Bose et al. 2019) significantly outclasses that of SN 2004dj. The nebular $H\alpha$ profile looks weird: two separated peaks of comparable intensity with the deep minimum in between. This $H\alpha$ profile unambiguously indicates the bipolar ^{56}Ni ejecta (Bose et al. 2019) presumably observed along the bipolar axis.

But this is not the only surprise demonstrated by SN 2016X. Even more unusual is the absence of the SN IIP generic [O I] 6300, 6364 Å nebular emission. This emission is barely seen on day 340 and completely absent at day 471 (Bose et al. 2019). At the moment this puzzling phenomenon remains a challenging problem.

Finally, we couldn't help noticing the unusual occultation effect due to the internal dust. On day 471 the red $H\alpha$ peak is significantly attenuated by the dust which signals the internal dust formation (Bose et al. 2019) at the right time for SNe IIP. On day 740 the red $H\alpha$ peak completely disappears which reflects the increase of the amount of the internal dust. The surprising fact however is that the blue $H\alpha$ peak does not show any sign of the additional blueshift caused by the occultation, which would be present in the case of the central (quasi-)spherical dusty zone likewise in SN 1987A (Lucy et al. 1989; Matsuura et al. 2017) and SN 1999em (Elmhamdi et al. 2003).

The unusual manifestations of SN 2016X raise a question, whether we see the explosion of a normal massive RSG with the progenitor mass and the explosion energy typical for explored SNe IIP, i.e., $M \sim 13 - 30 M_{\odot}$ and $E \sim (0.2-2) \times 10^{51}$ erg (Utrobin & Chugai 2017), or we face an extraordinary event. Fortunately, photometric and spectral observations (Huang et al. 2018; Bose et al. 2019) provide us with an excellent basis to explore different aspects of SN 2016X in detail and possibly to clear up the issue.

Below SN 2016X will be studied in several ways. We start with the hydrodynamic modelling to determine principal SN parameters, i.e., the ejecta mass, the kinetic energy, and the pre-SN radius; the amount of ^{56}Ni will be obtained directly from the luminosity in the radioactive tail. We then

recover the ^{56}Ni distribution in the envelope from the nebular double-peaked $H\alpha$ by means of the computation of the energy deposition produced by the asymmetric ^{56}Ni distribution. This simulation includes effects of the absorption of the $H\alpha$ emission by the dust, which will permit us to constrain the spatial distribution of the dusty material. Finally, we will use X-ray observations during the first 20 days after the explosion (Grupe et al. 2016; Bose et al. 2019) to infer the pre-SN wind density and to test a compatibility of the SN hydrodynamic parameters with the observational effects of the ejecta/wind interaction.

Throughout the paper we use the distance $D = 15.2 \pm 3.0$ Mpc (Bose et al. 2019) and the reddening $E(B - V) = 0.04$ mag (Huang et al. 2018). The explosion date is set to be 2016 January 18.7 that is recovered from the fit of the earliest V magnitudes by the hydrodynamic model. This moment is only 0.25 days earlier compared to that adopted by Huang et al. (2018).

2 HYDRODYNAMIC MODELLING

The principal SN parameters, i.e., the explosion energy, the ejecta mass, and the pre-SN radius are recovered via the hydrodynamic description of the observational bolometric light curve and the expansion velocity at the photosphere; the latter should be preferably fitted at the early photospheric stage, when the effects of the internal asymmetry of the radioactive ^{56}Ni ejecta are minimal. Another crucial parameter, the total amount of ^{56}Ni , is directly inferred from the flux at the early (<200days) stage of the radioactive tail. It is reasonable to start the section with clarifying the data that constitute the observational bases for the hydrodynamic modelling of SN 2016X.

2.1 Observational data

The available *UBVRI* photometry (Huang et al. 2018) is used to recover the bolometric light curve of SN 2016X. The filter fluxes are fitted by a black body spectrum multiplied by the reduction factor that takes into account the spectrum suppression in the blue and ultraviolet regions primarily due to the line opacity. The reduction factor depends on the SN age and its wavelength dependence is recovered from the SN 1987A spectral energy distribution at different ages (Pun et al. 1995). The photometric data taken by the 0.8-m Tsinghua University-NAOC telescope (TNT) and the Lijiang 2.4-m telescope (LJT) (Huang et al. 2018) are in good agreement and used to recover the observational bolometric light curve.

The time evolution of the observed photospheric velocity is taken from Huang et al. (2018). In addition to the photospheric velocity, we need the maximal velocity of the SN ejecta because of its key role in constraining hydrodynamic model. The point is that the maximal velocity is sensitive to the choice of the radius of the pre-SN model and its density structure. The earliest spectrum that provides us with a reliable value of the maximal velocity is the spectrum at 4.56 days. Our estimate of the velocity from the blue edge of the $H\alpha$ emission at that moment is 13750 ± 500 km s $^{-1}$, in accordance with the value reported by Huang et al. (2018, Fig. 10).

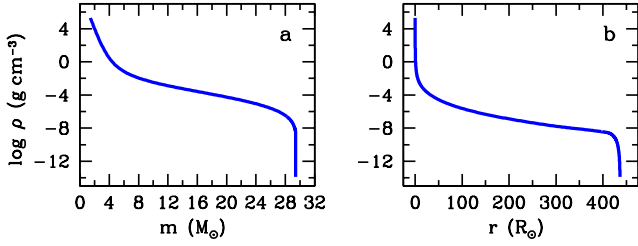


Figure 1. Density distribution as a function of interior mass (Panel a) and radius (Panel b) for the pre-SN model. The central core of $1.4 M_{\odot}$ is omitted.

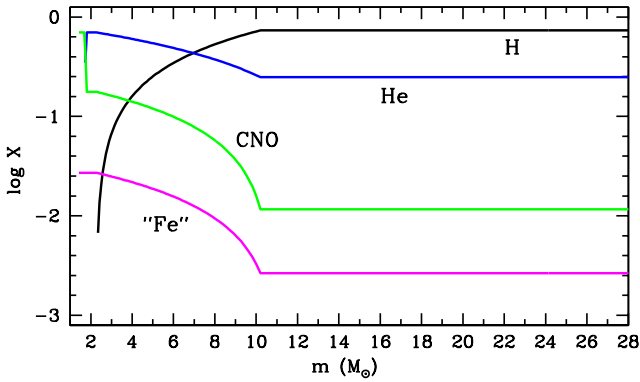


Figure 2. Mass fraction of hydrogen (black line), helium (blue line), CNO elements (green line), and Fe-peak elements excluding radioactive ^{56}Ni (magenta line) in the ejected envelope.

2.2 Model overview

The one-dimensional hydrodynamic code with the radiation transfer (Utrobin 2004) is used to explode the hydrostatic non-evolutionary pre-SN model. This approach is preferred because the pre-SN model produced by the stellar evolution computations is generally unable to describe SN IIP observations. This was understood in the wake of SN 1987A (Woosley 1988). A serious modification of the pre-SN model is required that includes the extended mixing between the metal-rich ejecta, the He-rich and H-rich envelopes with the smoothing of steep density gradients. The hand-made mixing is used therefore for the pre-SN model in order to imitate in the one-dimensional model the mixing produced by the real essentially three-dimensional explosion (Utrobin et al. 2017).

The acceptable pre-SN model is found via numerical simulations of a set of models with different SN parameters. The explosion of pre-SN model is initiated by a supersonic piston applied to the stellar envelope at the boundary with the collapsing $1.4 M_{\odot}$ core. The pre-SN density and chemical composition of the optimal model are shown in Fig. 1 and Fig. 2, respectively. We did not solve the optimization problem rigorously, since this procedure requires enormous computational efforts. Instead, the optimal model is recovered as a compromise between the fits to the observed light curve and the evolution of the velocity at the photosphere.

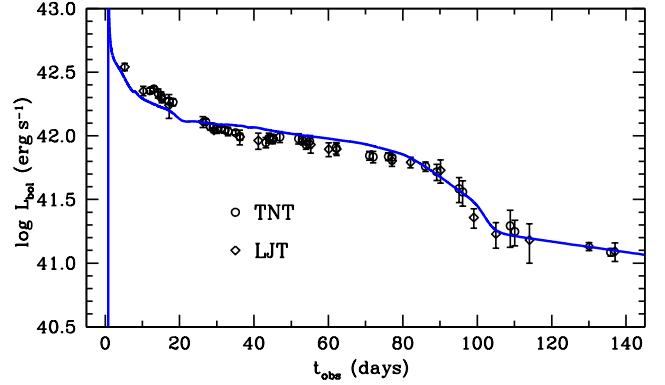


Figure 3. The model bolometric light curve (blue line) overplotted on the bolometric luminosities which we recovered from the photometric data reported by Huang et al. (2018).

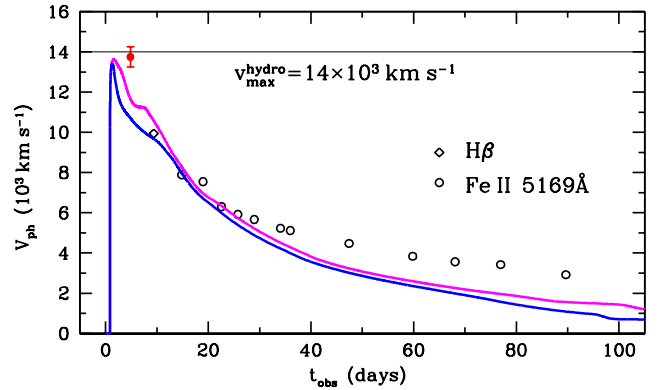


Figure 4. The evolution of model velocity at the photosphere defined by the level $\tau_{eff} = 2/3$ (blue line) and $\tau_T = 2/3$ (magenta line) is compared with the photospheric velocities estimated from the line absorption minimum (Huang et al. 2018). The red point is the early expansion velocity obtained from the blue wing of $H\alpha$. The horizontal line is the model maximal velocity corresponding to the strongest density peak formed at the shock breakout stage; the interaction with the wind is neglected. For the late-time mismatch see Section 2.3.

2.3 Optimal model and supernova parameters

The optimal hydrodynamic model satisfactorily reproduces the bolometric light curve (Fig. 3) and the expansion velocity at the early stage (Fig. 4). The model maximal velocity specified by the density peak at 14000 km s^{-1} (Fig. 5) is also consistent with the observed maximal velocity of $13750 \pm 500 \text{ km s}^{-1}$ recovered from the $H\alpha$ emission at 4.56 days. Note that both definitions of the photosphere via the effective and Thomson opacity predict close velocity values. The model V -band light curve fits satisfactorily the initial behavior of the absolute V magnitude including the discovery point (Fig. 6); the shown fit suggests that the explosion occurred at 2016 January 18.7, i.e., 0.25 days earlier compared to the explosion moment adopted by Huang et al. (2018).

The optimal model is specified by the ejecta mass $M = 28 M_{\odot}$, the kinetic energy $E = 1.73 \times 10^{51} \text{ erg}$, and the pre-SN radius $R_0 = 436 R_{\odot}$. The ^{56}Ni mass directly recovered from the radioactive tail is $0.0295 M_{\odot}$. The radial distribution of ^{56}Ni in the model is a spherical representation of the bipolar

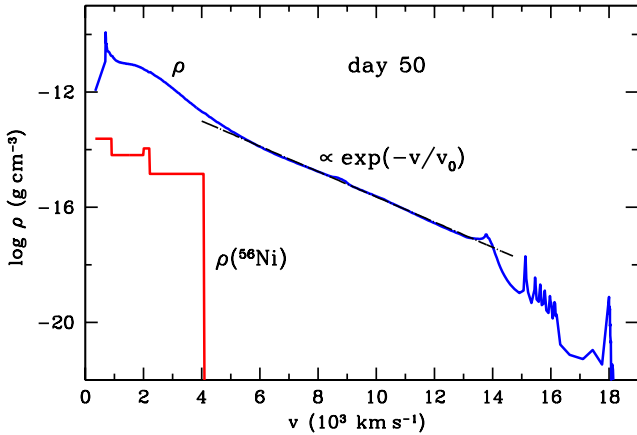


Figure 5. The gas (blue line) and ^{56}Ni (red line) density as a function of velocity at $t = 50$ days. Dash-dotted line is the exponential fit $\exp(-v/v_0)$.

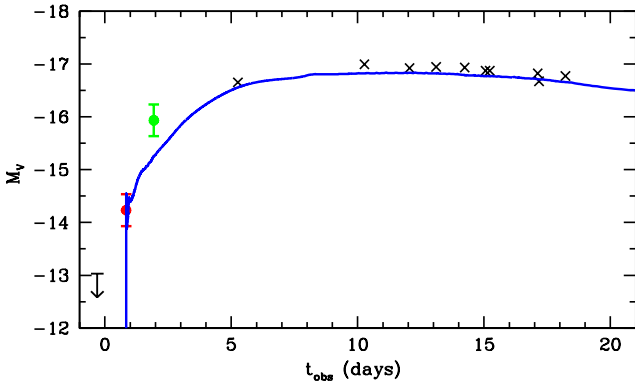


Figure 6. V-band light curve (blue line) during the first 20 days for the optimal model. Arrow marks the upper limit $V > 18.0$ mag for a non-detection on January 18.351, red point is the average of the two earliest V estimates separated by 0.008 days with the uncertainty of 0.3 mag, and green point is the V magnitude of 15.1 at January 20.586 (Bock et al. 2016). Crosses are the observational points of Huang et al. (2018). The model explosion date is January 18.7.

^{56}Ni ejecta recovered from the modelling of the $\text{H}\alpha$ profile at the nebular stage (Section 3). The total density and the density of ^{56}Ni in the freely expanding envelope is shown in Fig. 5. The oscillatory structure of the density distribution in the outermost layers ($v > 14000 \text{ km s}^{-1}$) forms at the shock breakout and is related to the instability of the radiative acceleration due to the strong opacity dependence on the temperature and density. The characteristic property of the optimal model is the large fraction of the kinetic energy residing in the outer layers: the $4 M_{\odot}$ external ejecta, about 14% of the total ejecta mass, contain about 50% of the total kinetic energy (Fig. 7). This feature is closely related to the ability of the hydrodynamic model to reproduce both the initial luminosity peak and the high expansion velocity of the external layers.

The uncertainty in the derived SN parameters can be estimated by a variation of the model parameters around the optimal model. The uncertainty of the distance (see Section 1) implies the 40% uncertainty in the bolometric

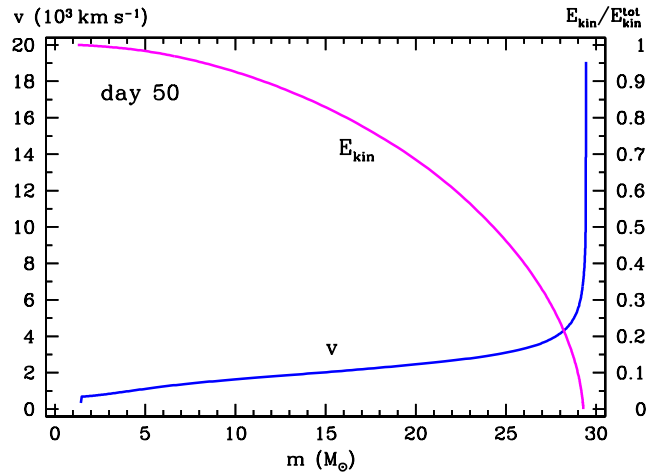


Figure 7. Distribution of velocity and kinetic energy along the mass coordinate in the SN ejecta of the optimal model on day 50.

luminosity. The scatter in the plot of the photospheric velocity versus time (Fig. 4) suggests the uncertainty of 7% in the photospheric velocity. We estimate the maximal uncertainty of the plateau length as 3 days, i.e., 3% of the plateau duration. With these uncertainties of observables, we find the errors of $\pm 360 R_{\odot}$ for the initial radius, $\pm 2.1 M_{\odot}$ for the ejecta mass, $\pm 0.19 \times 10^{51}$ erg for the explosion energy, and $\pm 0.012 M_{\odot}$ for the total ^{56}Ni mass.

The model reveals some deviations from the data, which require comments. The luminosity excess at the plateau (Fig. 3) stems from the spherical approximation of the bipolar ^{56}Ni distribution. Given the bipolar geometry of the ^{56}Ni ejecta, the escaping flux should be anisotropic at the late photospheric stage when the radioactivity contributes to the escaping luminosity. Furthermore, according to the $\text{H}\alpha$ model (Section 3), the rear ^{56}Ni component has larger both mass and velocity compared to the front component which implies that the backside photosphere is brighter than the front one. The observed “isotropic” luminosity ($4\pi D^2 f$) defined via the observed flux f thus underestimates the overall SN 2016X luminosity, which accounts for the model flux excess at the plateau. Another mismatch is the lower velocity at the photosphere compared to the observed values after about 30 days (Fig. 4). This disparity also stems from the spherical approximation of the ^{56}Ni distribution. Indeed, the bipolar ^{56}Ni ejecta result in the prolate shape of the photosphere with the large axis aligned along the line of sight. The observed velocities of absorption minima at the late plateau therefore are larger than the photospheric velocities of the spherical model.

2.4 Significance of early stage

The determination of SN IIP parameters is based on describing the bolometric or monochromatic light curves and the evolution of expansion velocity at the photospheric level by means of hydrodynamic modelling. It is obvious that the derived parameters are more reliable in the case of a SN IIP well observed photometrically and spectroscopically from the explosion moment till the radioactive tail. Here we would like to emphasize a significant role of the initial

($t < 30$ days) stage in recovering the SNe IIP parameters, because this issue is oftentimes missed.

The issue was partially explored for the well-observed SN 2005cs (Utrobin & Chugai 2008). The optimal hydrodynamic model in this case is characterized by the parameter set $M_{ej} = 15.9 M_{\odot}$, $E = 4.1 \times 10^{50}$ erg, and $R_0 = 600 R_{\odot}$. On the other hand, ignoring the fit to the initial stage permits us to describe the plateau of the light curve and the evolution of the photospheric velocity at the ages $t > 30$ days by the explosion of a $9 M_{\odot}$ pre-SN star with the parameters $M_{ej} = 7.8 M_{\odot}$, $E = 1.4 \times 10^{50}$ erg, and $R_0 = 700 R_{\odot}$ (Utrobin & Chugai 2008). Neglecting the early stage in the hydrodynamic modelling for SN 2005cs thus leads to a strong disagreement with the optimal model. A similar mismatch between the models with the full and reduced approaches was recently demonstrated for SN 1999em (see Utrobin et al. 2017, Fig. 13).

An alternative “easy-to-use” approach to estimate the basic SN IIP parameters is provided by the Litvinova-Nadyozhin relations between the parameters and the SN observables: the plateau duration, the luminosity and the photospheric velocity at the middle of the plateau (Litvinova & Nadezhin 1985). Although these relations are based on the extended grid of hydrodynamic models one should keep in mind that the models are not aimed at the description of the full data set on the bolometric light curve and the expansion velocities, so the parameters derived with this approach may differ by a significant factor from those determined via the hydrodynamic modelling of a particular SN IIP. Another drawback of this approach is neglecting the influence of radioactive ^{56}Ni on the light curve. The hydrodynamic parameters of the well-observed SN 1999em are $M_{ej} = 19 M_{\odot}$, $E = 1.3 \times 10^{51}$ erg, and $R_0 = 500 R_{\odot}$ (Utrobin 2007), whereas the Litvinova-Nadyozhin relations result in $M_{ej} = 15 M_{\odot}$, $E = 0.68 \times 10^{51}$ erg, and $R_0 = 414 R_{\odot}$ (Nadyozhin 2003), i.e., 20% lower ejecta mass and twice as low explosion energy. For SN 2016X the Litvinova-Nadyozhin relations suggest $M_{ej} = 23.5 M_{\odot}$, $E = 1.76 \times 10^{51}$ erg, and $R_0 = 130 R_{\odot}$, i.e., 16% lower ejecta mass and 3 times lower pre-SN radius compared to our optimal model.

To summarize, neglecting the description of the light curve and expansion velocities at the early epoch, $t < 30$ days, can significantly affect the SN IIP parameters inferred via the radiation hydrodynamic modelling of the RSG explosion in the framework of setting described above.

3 DOUBLE-PEAKED $\text{H}\alpha$ AND DUST DISTRIBUTION

The double-peaked $\text{H}\alpha$ profile in late nebular spectra of SN 2016X (Bose et al. 2019) is attributed to the bipolar ^{56}Ni ejecta embedded in the spherical hydrogen envelope. The striking feature of SN 2016X is that the $\text{H}\alpha$ peaks are fully separated by the deep minimum (Bose et al. 2019, Fig. 1) which indicates that we look at the supernova almost along the bipolar axis. On days 471 and 740 the $\text{H}\alpha$ is affected by the dust absorption: the red peak first gets weaker and on day 740 completely disappears. The model for the $\text{H}\alpha$ at late stages therefore should include absorption by the internal dust.

Table 1. Parameters of ^{56}Ni components.

Component	v_s	v_r	μ
	(km s $^{-1}$)		
front	1100	1100	1
rear	2400	1600	1.5
central	0	2000	0.075

The central to our model is the assumption that the bipolar ^{56}Ni ejecta do not disturb the overall hydrogen spherical symmetry. For the accepted bipolar ^{56}Ni distribution the gamma-ray energy deposition is calculated in the single flight approximation. The effective absorption coefficient for gamma-quanta of ^{56}Co decay is approximated as $k_{\gamma} = 0.06 Y_e \text{ cm}^2 \text{ g}^{-1}$, where Y_e is a number of electrons per nucleon (Kozma & Fransson 1992). Positrons of e^{-} -capture deposit their kinetic energy on-the-spot. The $\text{H}\alpha$ emissivity is assumed to be proportional to the local deposition rate; the emissivity saturation due to the complete ionization never attains at the relevant epochs.

The additional hydrogen ionization by the photoionization from the second level is neglected; this process however dominates at the early (195 days) nebular stage when the peaks contrast is relatively small and on day 142 when the double-peaked structure is not seen at all (Huang et al. 2018). The transformation between days 142 and 195 is related to the significant decrease of the rate of the hydrogen photoionization from the second level compared to the non-thermal ionization and excitation. On day 340 the photoionization from the second level is negligible, so the $\text{H}\alpha$ emissivity rate is uniquely linked with the local deposition of the energy of gamma-quanta and positrons of ^{56}Co decay, which favours the reliable inference of the ^{56}Ni distribution from the $\text{H}\alpha$ profile. The hydrogen abundance is assumed to be solar and homogeneous all over envelope except for the central region $v < v_h = 500 \text{ km s}^{-1}$ where no hydrogen is assumed. The density distribution of the homologously expanding envelope is exponential, $\rho = \rho_0 \exp(-v/v_0)$ with $\rho_0 \propto t^{-3}$ and v_0 determined by the ejecta mass of $28 M_{\odot}$ and the kinetic energy of 1.73×10^{51} erg.

The bipolar ^{56}Ni distribution is represented by the front and rear homogeneous spheres. We also tried homogeneous ellipsoids and cones but with less success. The central spherical component with the boundary velocity of 2000 km s^{-1} is also included. All the components lie on the same axis arbitrarily inclined by $i = 10^{\circ}$ with respect to the line of sight; in fact the observed profile admits the inclination angle of the bi-polar axis in the range of $i \lesssim 20^{\circ}$. Table 1 contains the derived shift (v_s), radius (v_r), and the relative mass of components for the optimal model (Fig. 8). Interestingly, the recovered bipolar structure is asymmetric: the mass and the shift velocity of the rear component are significantly larger compared to the front component (Table 1).

On days 471 and 740 the $\text{H}\alpha$ is strongly affected by the dust formed in the inner ejecta (Bose et al. 2019). Remarkably, an attempt to describe this effect in terms of the central dusty sphere, likewise it has been done in the case of SN 1987A (Lucy et al. 1989) and SN 1999em (Elmhamdi et al. 2003), fails (Fig. 8d). The dusty thick disk

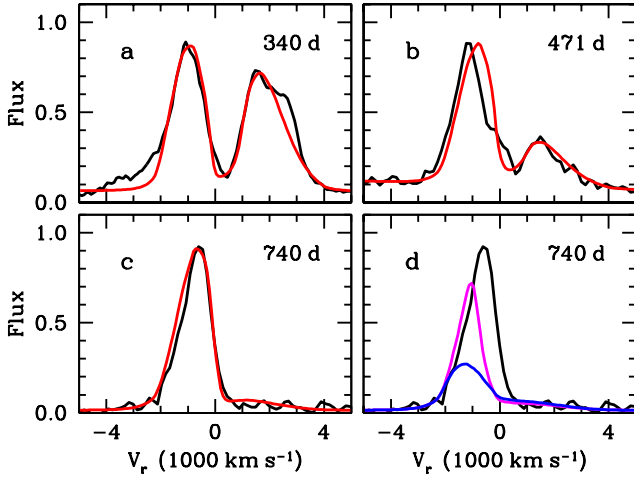


Figure 8. $H\alpha$ line in nebular spectra of SN 2016X (black line) with the overplotted profile of model (red line) in Table 1 on days 340, 471, and 740. Panel a: on day 340 the dust absorption is absent. Panel b: the spectrum on day 471 is reproduced by the same model as on day 340 that includes a geometrically thin dusty disk with the optical depth $\tau_d = 0.85$ shifted by 100 km s^{-1} towards far side (see Fig. 9). Panel c: the spectrum on day 740 with the same model as on day 471, but for the dust optical depth of 3. Panel d: the spectrum on day 740 cannot be reproduced with the dusty sphere (blue line) nor the geometrically thick dusty disk (magenta line).

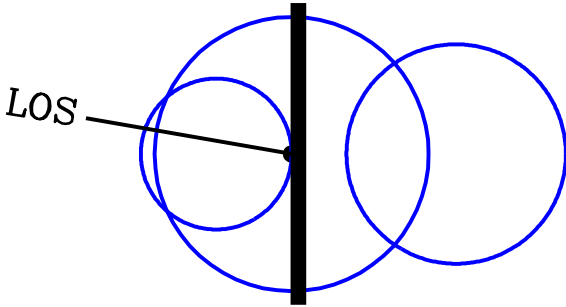


Figure 9. The configuration of the three homogeneous spheres of ^{56}Ni in the model of double-peaked $H\alpha$. The black vertical line section renders the dusty disk in the model of $H\alpha$ on day 740. Slanted line section shows the line of sight (LOS) assuming 10° inclination.

aligned perpendicular to the bipolar axis with the diameter/thickness ratio of 5 is also ruled out (Fig. 8d). While the red component can be fully absorbed for both dust configurations, the blue peak is modified by the dust absorption to an extent that makes both models unacceptable. The best fit on day 740 (Fig. 8c) is attained in the model with a thin dusty disk of the radius of 2200 km s^{-1} and the optical depth $\tau_d = 3$, aligned perpendicular to the bipolar axis and shifted by $\approx 100 \text{ km s}^{-1}$ towards rear component. It should be emphasized, that the model circular plane disk is an idealization. In reality this could be a non-circular irregular disk-like structure. On day 471 the same model requires the disk optical depth of 0.85 (Fig. 8b). The overall configuration of ^{56}Ni components with the model dusty disk is shown in Fig. 9.

It should be emphasized that the absence of the dust

Table 2. Parameters of Ca II components.

Component	v_s	v_r	μ
	(km s $^{-1}$)		
front	800	800	1
rear	2400	1600	0.2
central	0	2000	1.25

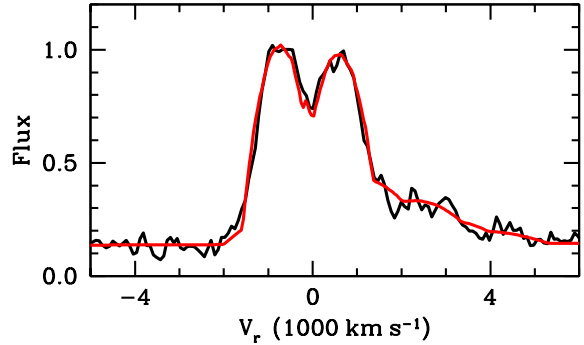


Figure 10. [Ca II] 7291, 7324 Å doublet in SN 2016X on day 340 (black line) with the overplotted model profile (red line) (Table 2) that demonstrates the dominance of the front component. Zero of radial velocity corresponds to the rest frame position of the 7281.47 Å line.

extinction on day 340 is consistent with the fact that the dust in SN 1987A and SN 1999em forms only after 400 days. This however raises a question, what is the origin of the blueshift of emission peaks of [Ca II] 7291, 7324 Å doublet reported by Bose et al. (2019). This cannot be the effect of the internal dust because even at the early nebular phase (195 days) the [Ca II] doublet shows the similar asymmetry. We suggest that the line asymmetry in the [Ca II] doublet is related to the asymmetry of the luminosity of the front and rear bi-polar components of [Ca II] emission. This possibility is illustrated in Fig. 10 that shows [Ca II] doublet on day 340 with the overplotted synthetic profile. The model includes three spherical components of homogeneous emissivity similar to the ^{56}Ni distribution. Models parameters, i.e., shift, radius, and relative luminosities of Ca II components are given in Table 2. These values emphasize the fact that the doublet luminosity of the front component is 5 times larger than rear one. This asymmetry can arise both from the different Ca masses or/and different ionization and excitation conditions in the front and rear components. The electron number densities in the components are comparable so, if the temperatures are also comparable, then the front component contains several times larger amount of Ca compared to the rear component. It might well be that the asymmetry of Ca components is the another manifestation of the asymmetry of ^{56}Ni components.

The model for [Ca II] profile includes additional parameter, the ratio R of blue-to-red emissivity that, in turn, depends on the line Sobolev optical depth. We find that the observed profile requires $R = 1.3$ (compared to $R = 1.5$ for the optically thin case). The recovered ratio corresponds to the optical depth in the 7291 Å line $\tau(7291\text{Å}) = 1.08$. Since the Ca II luminosity of the front component dominates and its

radius is minimal, the Ca II density is maximal in the front component. The recovered optical depth therefore refers primarily to the front component. The Sobolev optical depth can be converted to the Ca II mass of $1.1 \times 10^{-3} M_{\odot}$ for a given volume of the front component. Assuming a linear scaling between the mass and luminosity we obtain the total Ca II mass of three components of $\approx 2.7 \times 10^{-3} M_{\odot}$. Given a possible contribution of Ca III, (Ca II can be easily ionized by Ly α quanta) the found mass of Ca should be considered as the lower limit.

4 WIND DENSITY AND X-RAYS

The reported X-ray luminosity of SN 2016X (Bose et al. 2019) can be used to recover the density of the circumstellar (CS) gas lost by the pre-SN. To this end we employ the interaction model based on the thin shell approximation (Chevalier 1982; Giuliani 1982). The model was described earlier (Chugai et al. 2004) and we recap here only essential points. The gas swept up by the forward and reverse shock forms the shell whose expansion rate is governed by the equations of motion and mass conservation. The X-ray luminosity of both shocks at the moment t is calculated as the shock kinetic luminosity with the factor of the radiation efficiency $\eta = t/(t + t_c)$, where t_c is the cooling time of the postshock gas calculated for the density four times of the preshock density. The SN density distribution is set to be exponential $\rho = \rho_0 \exp(-v/v_0)$, which is in line with the hydrodynamic model (cf. Fig. 5). Parameters ρ_0 and v_0 are specified by the ejecta mass M_{ej} and the kinetic energy E . The escaping X-rays are subject to the absorption in the SN ejecta and in the cool dense shell that forms due to the cooling of shocked ejecta in the reverse shock. To compare the model X-ray luminosity with the observed values, we take into account only the X-ray radiation in the range $h\nu < 10$ keV in accordance with the reported *Chandra* and *Swift* data (Bose et al. 2019). The X-ray emission from the reverse shock gets into this band, while the relatively low contribution of the forward shock luminosity is taken into account adopting the spectrum $\epsilon^{-0.5} \exp(-\epsilon/kT)$.

The model X-ray luminosity reproduces the reported data (Fig. 11a) for the ejecta parameters $M_{ej} = 28 M_{\odot}$, $E = 2 \times 10^{51}$ erg, and the CS density distribution $\rho = \text{const}$ in the range of $r < 4 \times 10^{14}$ cm and $\rho \propto r^{-2}$ for larger radii (Fig. 11b, inset). The model boundary velocity of the unshocked ejecta well fits the velocity at 4.56 days found from the blue wing of the H α emission and the velocity at 28.8 days found from the blue edge of the H α absorption component (Fig. 11b). To summarize, the SN and CSM models reproduce both the X-ray data and the evolution of the maximal velocity of the unshocked ejecta. Yet it should be emphasized that the recovered CS density distribution can be also consistent with the other options of M_{ej} and E , provided their values obey the scaling $E \propto M_{ej}^{0.88}$.

The found wind density at $r > 4 \times 10^{14}$ cm is characterized by the parameter $w = \dot{M}/u = 1.9 \times 10^{14}$ g cm $^{-1}$. It is useful to express this parameter via convenient units as $w = \dot{M}_{-6}/u_{10} = 3$, where \dot{M}_{-6} is in units of $10^{-6} M_{\odot} \text{ yr}^{-1}$ and u_{10} is in units of 10 km s^{-1} . The inferred value $w = 3$ is three times as large as that for the type IIP SN 1999em and

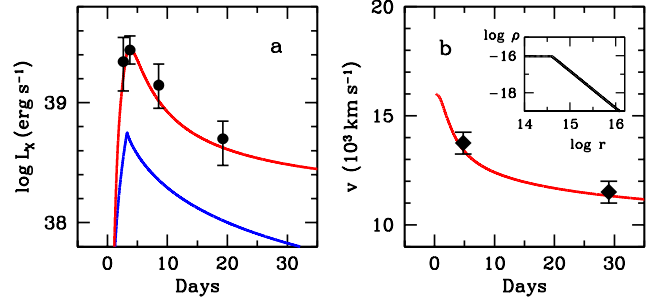


Figure 11. The X-ray luminosity in the range of < 10 keV and the boundary velocity of the unshocked ejecta for the CS interaction model. Panel **a**: the total escaping X-ray luminosity (red line) with contribution of the forward shock luminosity (blue line). Dots are the *Chandra* and *Swift* luminosity in 0.3 – 10 keV band (Bose et al. 2019). Panel **b**: the model boundary velocity of the unshocked ejecta (red line). Diamonds show the maximal velocity of the ejecta recovered from the H α blue emission wing on day 4.6 and from the blue edge of the H α absorption component at 28.8 days in the spectrum of Huang et al. (2018). Inset shows the CS density distribution.

Table 3. Hydrodynamic models of type IIP supernovae.

SN	R_0 (R_{\odot})	M_{ej} (M_{\odot})	E (10^{51} erg)	M_{Ni} ($10^{-2} M_{\odot}$)	$v_{\text{Ni}}^{\text{max}}$ (km s^{-1})	$v_{\text{H}}^{\text{min}}$ (km s^{-1})
1987A	35	18	1.5	7.65	3000	600
1999em	500	19	1.3	3.6	660	700
2000cb	35	22.3	4.4	8.3	8400	440
2003Z	230	14	0.245	0.63	535	360
2004et	1500	22.9	2.3	6.8	1000	300
2005cs	600	15.9	0.41	0.82	610	300
2008in	570	13.6	0.505	1.5	770	490
2009kf	2000	28.1	21.5	40.0	7700	410
2012A	715	13.1	0.525	1.16	710	400
2013ej	1500	26.1	1.4	3.9	6500	800
2016X	436	28.0	1.73	2.95	4000	760

SN 2004dj (Chugai et al. 2007). Since the mass-loss rate increases with the stellar mass one can conclude that the progenitor of SN 2016X was more massive compared to both mentioned SNe IIP. In order to find the RSG mass loss rate, one needs to know the wind velocity. The wind velocity of Milky Way RSGs with a mass of $\sim 30 M_{\odot}$ (e.g. μ Cep and VX Sgr) is 20 km s^{-1} (Mauron & Josselin 2011). Assuming the same wind velocity for SN 2016X, the mass-loss rate of its progenitor turns out to be $6 \times 10^{-6} M_{\odot} \text{ yr}^{-1}$.

5 DISCUSSION AND CONCLUSIONS

The recovered parameters of peculiar SN 2016X suggest rather high ejecta mass compared to other SNe IIP (Table 3) which were studied earlier on and whose parameters were summarized by Utrobin & Chugai (2017). Allowing for the collapsed core, the pre-SN mass amounts to $29.4 M_{\odot}$ which should be considered as a lower limit for the main-sequence mass of the progenitor. The mass lost by the BSG wind during the main-sequence phase can be estimated unfortunately only with a large uncertainty. The theoretical

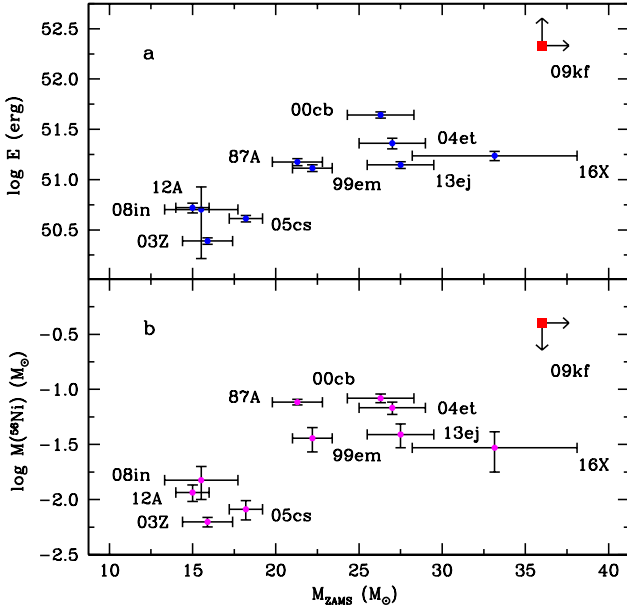


Figure 12. Explosion energy (Panel a) and ^{56}Ni mass (Panel b) vs. hydrodynamic progenitor mass for SN 2016X and ten other core-collapse SNe (Utrobin & Chugai 2017).

bolometric luminosity of a $30 M_{\odot}$ progenitor is $\approx 4 \times 10^5 L_{\odot}$ (e.g. Eldridge et al. 2013). Observational mass-loss rate for a BSG of that luminosity lies in the range from 5×10^{-8} to $\sim 10^{-6} M_{\odot} \text{ yr}^{-1}$ (cf. Krtićka & Kubát 2017). Given the lifetime at the hydrogen burning stage of about $6 \times 10^6 \text{ yr}$ (Meynet et al. 1994), the lost mass thus turns out in the range of ~ 0.3 to $\sim 6 M_{\odot}$. At the RSG stage, the recovered mass-loss rate of about $6 \times 10^{-6} M_{\odot} \text{ yr}^{-1}$ and the RSG lifetime of $\approx 10^5 \text{ yr}$ (Meynet et al. 2015) result in the lost mass of $\sim 0.6 M_{\odot}$. The total mass lost by the progenitor thus lies in the range of 0.9 to $6.6 M_{\odot}$. These values combined with the error of the ejecta mass are translated into the SN 2016X progenitor mass range from 28.2 to $38.1 M_{\odot}$. Even with the minimal progenitor mass of about $30 M_{\odot}$, SN 2016X turns out the most massive among normal SNe IIP on the scatter diagrams E vs. M_{ZAMS} and $M(^{56}\text{Ni})$ vs. M_{ZAMS} (Fig. 12). We speculate that the large progenitor mass could be somehow related to peculiar manifestations of SN 2016X including the bipolar structure of the ^{56}Ni ejecta, the low luminosity of the [O I] doublet, and the unusual disk-like distribution of the dusty material.

The pronounced bipolar ^{56}Ni ejecta is likely produced by the bipolar explosion asymmetry. Factors that favored this asymmetry could include a large scale instability at the core collapse or/and a rotation. It is likely that the dusty disk-like structure is also an outcome the bipolar asymmetry. This structure could be related to either the dense two-dimensional condensation in the equatorial plane formed during the explosion, or the fragment of the dense shell of the ^{56}Ni bubble in the far hemisphere.

The absence of the normal [O I] emission might be explained by the low amount of the synthesized oxygen in the ejected envelope. There could be two reasons for that: (i) the low-mass progenitor $M_{ZAMS} \approx 10 M_{\odot}$ with the pre-SN devoid of the oxygen mantle around the collapsing core, or (ii) the fallback of the oxygen shell onto the black hole. The

first possibility should be discarded since it contradicts to the large ejecta mass. The second option cannot be ruled out because we are not aware of the explosion details.

An alternative possibility is that the O-rich matter in SN 2016X ejecta is too cold for the normal [O I] emission. This situation could arise, if CO and SiO molecules are formed at the nebular stage all over the oxygen ejecta. The conjecture follows the findings that the cooling of the O-rich matter via CO and SiO molecules in SN 1987A strongly suppresses the nebular [O I] emission, so the observed [O I] emission comes out only from the oxygen matter devoid of molecules (Liu & Dalgarno 1995). For SN 2016X the luminosity of the [O I] 6300, 6364 Å on day 340 is $\leq 7.7 \times 10^{37} \text{ erg s}^{-1}$ according to the spectrum reported by Bose et al. (2019). The oxygen-core mass of a $30 M_{\odot}$ progenitor is of $8 M_{\odot}$ (Woosley et al. 2002). Taking into account the collapsed $1.4 M_{\odot}$ core and assuming the solar C/O ratio, we obtain the $4.6 M_{\odot}$ oxygen ejecta. The luminosity of the [O I] doublet from this amount of oxygen meets the observation constraint, if the excitation temperature of the oxygen is $\leq 2000 \text{ K}$. This requirement is easily fulfilled since the temperature in the oxygen zone of SN 1987A cooled by CO and SiO molecules is about 1800 K during the first year and later on gets lower (Liu & Dalgarno 1995). The SN 2016X is presumably a special case in which CO and SiO molecules form throughout the O-rich matter. This assumption combined with a moderate amount of ^{56}Ni would result in the strong cooling of all the O-rich gas thus inhibiting [O I] emission. One may conjecture that the required Si and O abundance in the oxygen-rich matter is the outcome of the He and C burning in combination with the convection and rotation-induced mixing (e.g. Heger 1998). If the efficient CO and SiO cooling occurs in SN 2016X, one expects that similar high-mass SNe IIP at the nebular stage should demonstrate a strong CO and SiO emission in the vibrational fundamental and first overtone bands.

The recovered mass of the SN 2016X ejecta aggravates the well-known disparity between the relatively high masses of SN IIP progenitors estimated by means of the hydrodynamic modelling of the well-observed SNe IIP (Table 3) and the lower progenitor masses inferred from the archival photometry using the stellar evolution models. At the moment the stellar evolution theory is unable to reliably fix the upper boundary of the mass range producing SNe IIP, M_{IIP} , because the resulting loss of the hydrogen envelope is a matter of the adopted prescription for mass loss and rotation effects. Recent evolutionary calculations of massive stars suggest that $M_{\text{IIP}} \sim 20 M_{\odot}$ at the solar metallicity without rotation (Limongi & Chieffi 2018). This is lower than the former estimate of ~ 30 – $35 M_{\odot}$ (Limongi & Chieffi 2010). The reassessment is caused by a high mass-loss rate taken from van Loon et al. (2005). However, one should keep in mind that this mass-loss prescription suffers from large uncertainties. Particularly, it predicts a larger mass-loss rate by a factor of about 1.8 dex compared to that of the well-studied Galactic RSG $\alpha \text{ Ori}$ and $\mu \text{ Cep}$ (van Loon et al. 2005, Figure 11). The situation with the value of M_{IIP} predicted by the theory of stellar evolution thus looks rather uncertain with the conservative estimate of M_{IIP} in the range of 20 – $35 M_{\odot}$ for stars with the solar metallicity and zero rotation velocity.

ACKNOWLEDGEMENTS

We thank Subo Dong for kindly sharing spectra of SN 2016X. V.P.U. is partially supported by Russian Scientific Foundation grant 19-12-00229.

REFERENCES

- Bisnovatyi-Kogan G. S., 1971, *Soviet Ast.*, **14**, 652
- Bisnovatyi-Kogan G. S., Moiseenko S. G., Ardelyan N. V., 2018, *Physics of Atomic Nuclei*, **81**, 266
- Bock G., et al., 2016, *The Astronomer's Telegram*, 8566
- Bose S., et al., 2019, *ApJ*, **873**, L3
- Burrows A., Dessart L., Livne E., Ott C. D., Murphy J., 2007, *ApJ*, **664**, 416
- Chevalier R. A., 1982, *ApJ*, **259**, 302
- Chugai N. N., 2007, in Immler S., Weiler K., McCray R., eds, *American Institute of Physics Conference Series Vol. 937, Supernova 1987A: 20 Years After: Supernovae and Gamma-Ray Bursters*. pp 357–364, doi:10.1063/1.3682929
- Chugai N. N., Chevalier R. A., Lundqvist P., 2004, *MNRAS*, **355**, 627
- Chugai N. N., Fabrika S. N., Sholukhova O. N., Goranskij V. P., Abolmasov P. K., Vlasyuk V. V., 2005, *Astronomy Letters*, **31**, 792
- Chugai N. N., Chevalier R. A., Utrobin V. P., 2007, *ApJ*, **662**, 1136
- Eldridge J. J., Fraser M., Smartt S. J., Maund J. R., Crockett R. M., 2013, *MNRAS*, **436**, 774
- Elmhamdi A., et al., 2003, *MNRAS*, **338**, 939
- Giuliani Jr. J. L., 1982, *ApJ*, **256**, 624
- Grassberg E. K., Imshennik V. S., Nadyozhin D. K., 1971, *Ap&SS*, **10**, 28
- Grupe D., Dong S., Shappee B. J., Holoien T., Stanek K., Kochanek C., Prieto J. L., Margutti R., 2016, *The Astronomer's Telegram*, 8588, 1
- Heger A., 1998, PhD thesis, Max-Planck Institute for Astrophysics <EMAIL>alex@ucolick.org</EMAIL>
- Heger A., Fryer C. L., Woosley S. E., Langer N., Hartmann D. H., 2003, *ApJ*, **591**, 288
- Huang F., et al., 2018, *MNRAS*, **475**, 3959
- Janka H.-T., 2017, *Neutrino-Driven Explosions*. p. 1095, doi:10.1007/978-3-319-21846-5_109
- Kozma C., Fransson C., 1992, *ApJ*, **390**, 602
- Krtićka J., Kubát J., 2017, *A&A*, **606**, A31
- LeBlanc J. M., Wilson J. R., 1970, *ApJ*, **161**, 541
- Limongi M., Chieffi A., 2010, in *Journal of Physics Conference Series*. p. 012002, doi:10.1088/1742-6596/202/1/012002
- Limongi M., Chieffi A., 2018, *ApJS*, **237**, 13
- Litvinova I. Y., Nadezhin D. K., 1985, *Soviet Astronomy Letters*, **11**, 145
- Liu W., Dalgarno A., 1995, *ApJ*, **454**, 472
- Lucy L. B., Danziger I. J., Gouiffes C., Bouchet P., 1989, in *Tenorio-Tagle G., Moles M., Melnick J., eds, Lecture Notes in Physics, Berlin Springer Verlag Vol. 350, IAU Colloq. 120: Structure and Dynamics of the Interstellar Medium*. p. 164, doi:10.1007/BFb0114861
- Matsuura M., et al., 2017, *MNRAS*, **469**, 3347
- Mauerhan J. C., et al., 2017, *ApJ*, **834**, 118
- Mauron N., Josselin E., 2011, *A&A*, **526**, A156
- Meynet G., Maeder A., Schaller G., Schaerer D., Charbonnel C., 1994, *A&AS*, **103**, 97
- Meynet G., et al., 2015, *A&A*, **575**, A60
- Nadyozhin D. K., 2003, *MNRAS*, **346**, 97
- Pumo M. L., Zampieri L., Spiro S., Pastorello A., Benetti S., Cappellaro E., Manicò G., Turatto M., 2017, *MNRAS*, **464**, 3013
- Pun C. S. J., et al., 1995, *ApJS*, **99**, 223
- Smartt S. J., 2009, *ARA&A*, **47**, 63
- Smartt S. J., 2015, *Publ. Astron. Soc. Australia*, **32**, e016
- Utrobin V. P., 2004, *Astronomy Letters*, **30**, 293
- Utrobin V. P., 2007, *A&A*, **461**, 233
- Utrobin V. P., Chugai N. N., 2008, *A&A*, **491**, 507
- Utrobin V. P., Chugai N. N., 2017, *MNRAS*, **472**, 5004
- Utrobin V. P., Chugai N. N., Pastorello A., 2007, *A&A*, **475**, 973
- Utrobin V. P., Chugai N. N., Botticella M. T., 2010, *ApJ*, **723**, L89
- Utrobin V. P., Wongwathanarat A., Janka H.-T., Müller E., 2017, *ApJ*, **846**, 37
- Wheeler J. C., Meier D. L., Wilson J. R., 2002, *ApJ*, **568**, 807
- Woosley S. E., 1988, *ApJ*, **330**, 218
- Woosley S. E., Heger A., Weaver T. A., 2002, *Reviews of Modern Physics*, **74**, 1015
- van Loon J. T., Cioni M. R. L., Zijlstra A. A., Loup C., 2005, *A&A*, **438**, 273

This paper has been typeset from a $\text{\TeX}/\text{\LaTeX}$ file prepared by the author.